ELSEVIER

Flow channeling in a single fracture induced by shear displacement

Harold Auradou [a,*], German Drazer [b,c], Alejandro Boschan [a,d],
Jean-Pierre Hulin [a], Joel Koplik [b]

[a] *Laboratoire Fluides, Automatique et Systèmes Thermiques, UMR 7608, CNRS, Universités Paris 6 and 11,
Bâtiment 502, Campus Paris Sud, 91405 Orsay Cedex, France*
[b] *Benjamin Levich Institute, Department of Physics, City College of the City University of New York,
New York, NY 10031, USA*
[c] *Department of Chemical & Biomolecular Engineering, Johns Hopkins University,
Baltimore, MD 21218, USA*
[d] *Grupo de Medios Porosos, Facultad de Ingenieria, Paseo Colon 850,
1063 Buenos Aires, Argentina*

Abstract

The effect on the transport properties of a fracture of a shear displacement $\vec{u}$ between its complementary surfaces is investigated experimentally and numerically. The shear displacement $\vec{u}$ induces an anisotropy of the fracture aperture field with a correlation length scaling of $|\vec{u}|$, which is significantly larger in the direction perpendicular to $\vec{u}$. This reflects the presence of long fluid flow channels perpendicular to the shear displacement, resulting in a higher effective permeability in that direction. Such channels will have a strong influence on the transport characteristics of a fracture, such as, for instance, its thermal exchange area, crucial for geothermal applications. Miscible displacement fronts in shear-displaced fractures obtained experimentally display a self-affine geometry with a characteristic exponent directly related to that of the fracture surfaces. We present a simple model, based on the channeling of the aperture field, which reproduces the front geometry when the mean flow is parallel to the channels created by the shear displacement.
© 2006 CNR. Published by Elsevier Ltd. All rights reserved.

Keywords: Fracture; Self-affine; Fractal; Permeability; Hydrodynamic; Mixing; Dispersion; Hot dry rock

* Corresponding author. Tel.: +33 1 69 15 80 41; fax: +33 1 69 15 80 60.
  E-mail address: auradou@fast.u-psud.fr (H. Auradou).

1. Introduction

The reservoir at the Soultz-sous-Forêts Hot Dry Rock (HDR) site, like many geological systems, contains a complex fracture network. Such networks often display preferential flow paths, at the scale of the entire network and of a single fracture. In both cases, identifying these preferential transport paths is crucial for geothermal applications. At the fracture network scale, the number of hydraulically connected fractures and their spatial distribution largely determine the rate at which fluids can be produced from, and re-injected into, a geothermal system (Genter et al., 1997; Dezayes et al., 2004). At the single fracture scale, the effective thermal exchange area will strongly depend on the flow field inside the fracture; it may be significantly larger when flow is evenly distributed across the entire fracture area than when it is localized in a few preferential channels. Understanding the flow distribution is therefore the first essential step towards modeling heat exchange in an HDR reservoir. In this work we focus on the effect that a relative shear displacement of the fracture walls has on the spatial variations of the fracture aperture and, as a result, on the fluid flow velocity field. Such shear displacements are frequently induced in geothermal fields by hydraulic stimulation operations using the massive injection of water at high flow rates to increase the overall transmissivity of the fractures, as shown by borehole and microseismic observations (Genter et al., 1997; Evans et al., 2005).

We will analyze, at the scale of a single fracture, the influence of shear displacements of the fracture walls on the pore space structure and, hence, on the transport properties. Specifically, we investigate the case of fractures with a self-affine geometry, which corresponds to a statistical model that successfully describes fracture geometry, including the occurrence of long-range spatial correlations, for a broad variety of fractured materials [see Bouchaud (2003) for a review]. An important factor in these processes is the anisotropy of the permeability field induced by the shear displacement of the fracture walls; the permeability is highest for flow perpendicular to the shear displacement vector $\vec{u}$ and lowest along it (Gentier et al., 1997; Yeo et al., 1998). Auradou et al. (2005) have suggested that this anisotropy is related to the presence of ridges perpendicular to $\vec{u}$ in the aperture field. These ridges partially inhibit flow parallel to $\vec{u}$ and create preferential flow channels connected in series in the perpendicular direction, suggesting that the pore space might be modeled as long parallel channels extending over the length of the fracture.

The validity of this simple description of the void space is confirmed here by a detailed study of the geostatistical characteristics of the aperture field. It is shown that the anisotropy of the aperture field and the presence of large-scale surface structures spanning the whole surface are both needed to account for the anisotropic permeability of a fracture.

The previous analysis will then be extended to the spreading of a tracer advected by the flowing fluid. This process is largely determined by the structure of the flow field, which at first glance seems to be very complex. Laboratory experimental studies (Auradou et al., 2001) and numerical simulations (Drazer et al., 2004) suggest, however, that, for shear displacements that are small compared to the size of the fracture and for an average flow that is perpendicular to $\vec{u}$, the flow lines are mostly parallel to the mean flow direction. In other words, the velocity field remains correlated over distances of the order of the fracture length. Such large correlation lengths may strongly influence solute dispersion and other transport properties such as heat transfer. Finally, the correlation of the velocity of tracer particles advected in the fracture will be shown to have self-affine characteristics, and a model accounting for the geometry of miscible displacement fronts in such fractures will be presented.
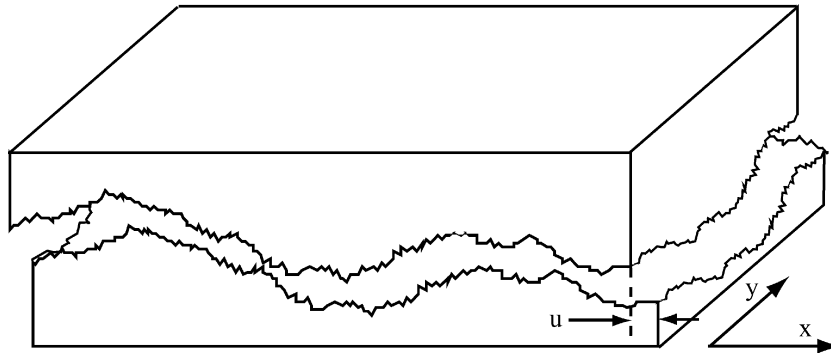
Fig. 1. Schematic view of the experimental fracture models. The fracture walls are complementary surfaces with the same roughness geometry and self-affine exponent $\xi \sim 0.8$ as found in natural granite fractures. The model walls are shifted vertically to determine the mean aperture and horizontally to model relative shear displacements. *u*: amplitude of shear.

2. Experimental setup and numerical models

Both in the laboratory experiments and in the numerical simulations, the fractures are modeled as the gap between two complementary rough surfaces as shown in Fig. 1. Experimentally, these surfaces are transparent epoxy casts of granite blocks or fracture surfaces that retain their self-affine geometry. The experimental setup allows us to control both the normal distance and the lateral displacement between the two facing wall surfaces; a detailed description can be found in Auradou et al. (2001, 2005). Note that all dimensions in this paper are given in millimeters.

The normal distances investigated range from 0.5 to 1 mm, i.e. of the same order of magnitude as the mean aperture of fractures in the Soultz HDR reservoir (Sausse, 2002). The lateral displacement mimics a relative shear displacement of the fracture walls and induces spatial variations in their apertures. The magnitude of the shear displacements ranges from zero (no-shear configuration) to a few millimeters (the lateral displacement brings the opposite surfaces into contact). The amplitude of the shear displacements is of the same order of magnitude as those estimated by Evans et al. (2005) after hydraulic stimulation of the fractures at Soultz. The resulting aperture fluctuations are also similar to those reported by Sausse (2002) for fractures in the Soultz HDR reservoir.

In the laboratory the fracture model is placed inside a rectangular basin and both the model and the basin are initially saturated with a transparent solution, making sure that no air bubbles are trapped inside the system. The same solution, but dyed, is then injected through a small borehole in the center of the upper epoxy cast, and photographs of the dye invasion front are taken at regular time intervals. Figure 2 depicts a typical invasion front geometry: its larger elongation in the direction perpendicular to the shear displacement reflects the permeability anisotropy mentioned earlier. Moreover, as discussed by Auradou et al. (2005), the ratio of the elongations of the front parallel and perpendicular to the shear is directly related to the ratio of the permeabilities.

As indicated above, aperture variations due to the lateral displacement of the fracture walls strongly perturb the flow field. Numerical simulation of the experiments therefore entails an accurate 3D description of the fracture geometry and the velocity field. The lattice Boltzmann technique was selected for this purpose since it is particularly suited to handling complex geometries (Drazer and Koplik, 2000, 2002). A large cubic lattice ($1024 \times 1024 \times 20$ nodes) is used to reproduce a model fracture with a mean aperture of 1 mm and an area of $51.2 \, \text{mm} \times 51.2 \, \text{mm}$ (a quarter of the area used in the laboratory experiments). The variability of the numerical simulation results from one fracture to the next was investigated and the permeabilities for flow parallel and
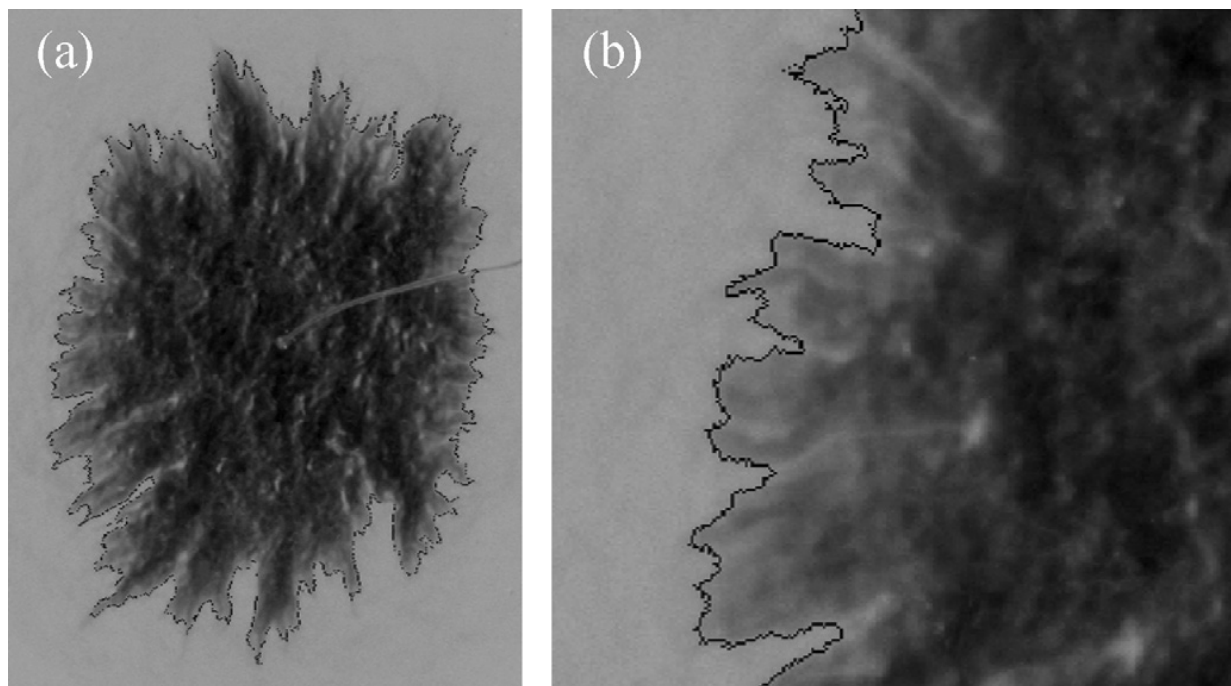
Fig. 2. Photographs showing laboratory experiment results. (a) Radial injection of a dyed fluid into a fracture saturated with a miscible, transparent fluid (190 mm × 142 mm); (b) detail of the invasion front (62 mm × 62 mm).

perpendicular to the shear direction were determined (note that only their ratio can be measured experimentally).

The aperture fields corresponding to relative displacements of the same complementary surfaces in two right-angle directions are compared in Fig. 3. Permeability values computed in these two cases for constant pressure gradients oriented parallel and perpendicular to the shear are given in this figure. The near continuous streaks perpendicular to the shear displacement visible in the figure correspond to preferential flow paths. As will be shown later, these paths strongly enhance solute dispersion and may also affect other transport properties such as heat transfer between the flowing fluid and the fracture walls. For instance, if the velocity contrasts are high enough and wide low-velocity zones appear, the effective heat transfer area may be significantly reduced.

The occurrence of the preferential flow paths is reflected in the difference in the permeabilities $K_{//}$ and $K_{\perp}$, corresponding to flows parallel and perpendicular to the channels, respectively. More precisely, the permeability $K_{\perp}$ for flow perpendicular to the displacement increases with $|\vec{u}|$, while $K_{//}$ decreases. These changes in the permeability of the fracture are related to the permeability K_0 (for $|\vec{u}| = 0$) and to the ratio S of the variance of the aperture fluctuations, σ_a, to the mean aperture, a_0, through the following approximations (Auradou et al., 2005):

$$\frac{K_{\perp}}{K_0} = 1 + 3AS^2 \tag{1}$$

$$\frac{K_{//}}{K_0} = 1 - 6BS^2 + O(S^4) \tag{2}$$

The two constants, A and B, depend on the specific statistical properties of each individual fracture but, in general, satisfy the relations $A < 1$ and $B < 1$. Eq. (2) results from a development in which terms of order 4 and higher, i.e. $O(S^4)$, are neglected.

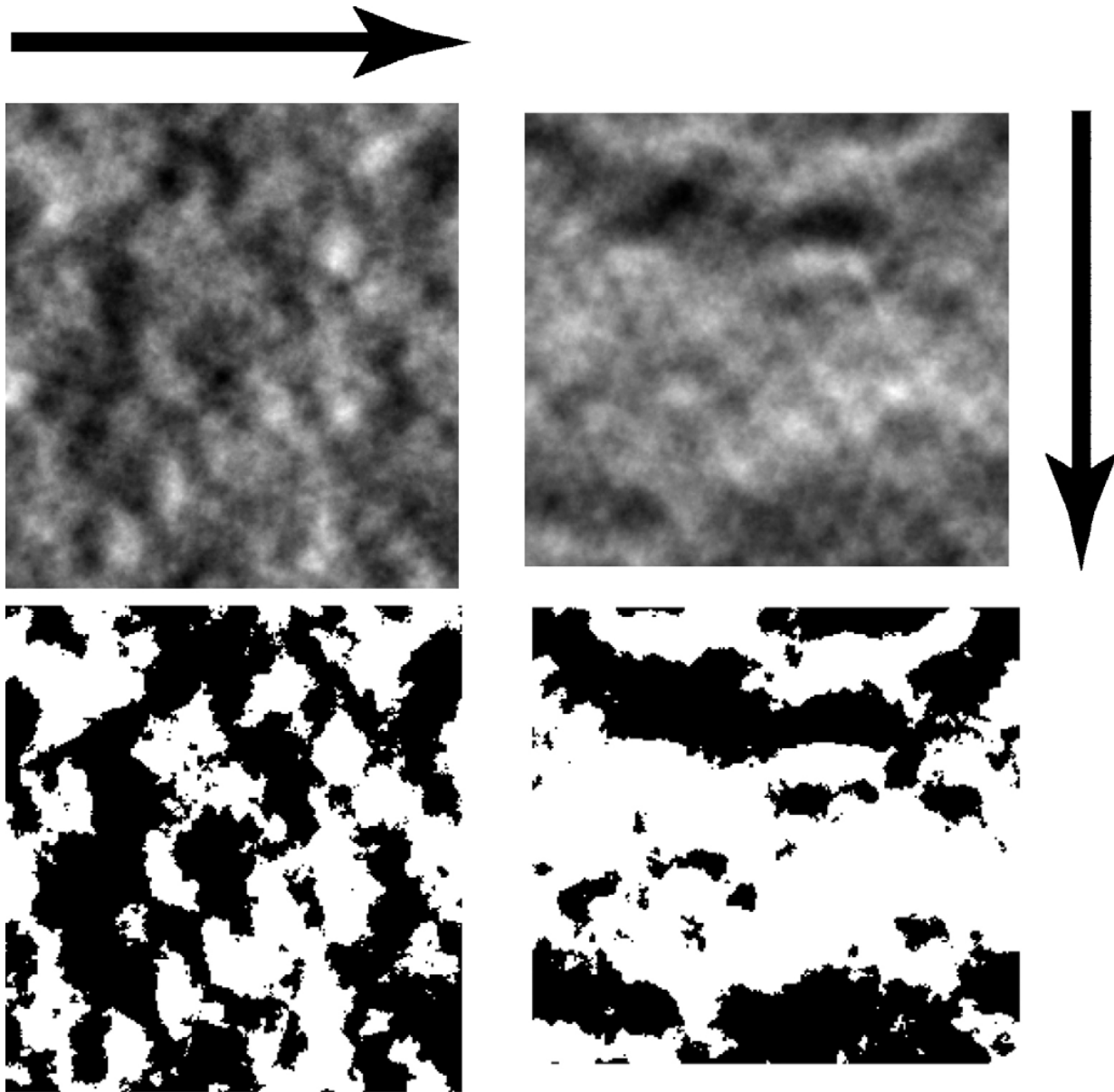Fig. 3. Numerical aperture fields (51.2 mm × 51.2 mm) obtained for the same magnitude of shear displacement $\vec{u}$ ($u = 0.8$ mm) along two different perpendicular directions, as indicated by the arrows. Upper images: aperture fields coded in tones of grey; lower images: binary images corresponding to a 1 mm threshold equal to the mean aperture (smallest apertures shown in white). Left: $S = 0.16$, $K_\perp/K_0 = 1.05$ and $K_{//}/K_0 = 0.822$ ($S =$ ratio of the variance of the aperture fluctuations and the mean aperture, $K_{//}$ and $K_\perp =$ permeability values for flow parallel and perpendicular to the shear displacement $\vec{u}$, $K_0 =$ permeability for $u = 0$). Right: $S = 0.21$, $K_\perp/K_0 = 1.00$ and $K_{//}/K_0 = 0.930$.

The aperture fields shown in Fig. 3 display ridges perpendicular to the displacement $\vec{u}$ and extend over a large part of the fracture length. This observation forms the basis of a simple model in which the aperture field is replaced by a set of parallel channels, each of constant aperture and perpendicular to the direction of shear. The model captures the linear dependence of the permeabilities with respect to S^2 and gives a good estimate of the respective upper and lower boundaries of $K_\perp$ and $K_{//}$ (Zimmerman et al., 1991; Zimmerman and Bodvarsson, 1996; Auradou et al., 2005). The two limits correspond to $A = 1$ and $B = 1$ in Eqs. (1) and (2). This simple model takes advantage of the fact that the correlation length in the aperture field is highly anisotropic. Specifically, the correlation length is substantially smaller in the direction parallel to

$\vec{u}$. In addition to its global anisotropy, the photos taken during the experiment (Fig. 2) also show that the displacement front, between the transparent and dyed fluids, is locally quite tortuous. Its geometry was indeed found experimentally to be self-affine with a characteristic exponent (ζ) close to that of the roughness of the fracture surfaces (Auradou et al., 2001). This result was verified numerically by Drazer et al. (2004) for two values of the characteristic exponent ζ (0.8 and 0.5).

The spatial correlation of the aperture and the velocity fields in these fractures will be analyzed quantitatively in Section 3, using standard statistical tools. A model relating the corresponding statistical parameters to characteristics of the displacement front geometry will then be derived in Section 4. It will be shown to capture the key features of the results of both the laboratory experiments and the numerical simulations.

3. Spatial correlation of the fracture aperture field

An analysis was performed on 2D maps of the aperture field (770×760 pixels), measured in the epoxy surfaces with a mechanical profilometer; the spacing between pixels is 0.250 mm in both directions of the mean plane of the fracture; the vertical resolution on the local height $h(x, y)$ is 0.01 mm. The statistical properties of the surface roughness were determined from these maps and can be characterized in terms of a self-affine geometry. The main property of a self-affine surface is that it remains statistically unvaried under the transformation:

$$x \rightarrow \lambda x, \qquad y \rightarrow \lambda y, \qquad h(x, y) \rightarrow \lambda^\zeta h(x, y)$$

where (x, y) are the coordinates in the mean surface plane, $h(x, y)$ the local height of the surface, and ζ is the Hurst, roughness, or self-affine exponent (Feder, 1988). For the fractures used in the laboratory, $\zeta = 0.75 \pm 0.05$ (Auradou et al., 2005), in agreement with published values for granite surfaces (Bouchaud, 2003). In the simulations, the self-affine surfaces are generated numerically [see Drazer and Koplik (2002) for a detailed description of the method]. In our study, we consider fractures made of complementary walls that are separated vertically, to open the fracture, and laterally, to mimic shear displacements (if any). Under such conditions, if a_0 and $\vec{u}$ are, respectively, the relative normal and shear displacements of the fracture walls, the local aperture at a point $\vec{r}$ is given by

$$a(\vec{r}) = h(\vec{r}) - h(\vec{r} + \vec{u}) + a_0 \tag{3}$$

Eq. (3) allows us to determine from the experimental surface map $h(\vec{r})$ the aperture field $a(\vec{r})$ for any given shift $\vec{u}$. The correlations in the aperture field are characterized by the following correlation function, or semivariance (γ) (Kitanidis, 1997):

$$\gamma(\vec{\delta}) = \langle [a(\vec{r}) - a(\vec{r} + \vec{\delta})]^2 \rangle \tag{4}$$

that gives the spatial correlation of the aperture field between two points separated by the 2D vector $\vec{\delta}$. The brackets correspond to an average done over all pairs of points separated by a lag vector $\vec{\delta}$. The variation of γ with $\vec{\delta}$ allows to characterize the distance over which the aperture variations are correlated.

Combining Eqs. (3) and (4), one observes that the value of γ is determined by the correlation between the heights of the surface at four points located at the corners of a parallelogram of sides $\vec{u}$ and $\vec{\delta}$. The cases in which the lag $\vec{\delta}$ is parallel or perpendicular to the shear displacement $\vec{u}$ are of special interest (from here on they are referred to as // and $\perp$, respectively).
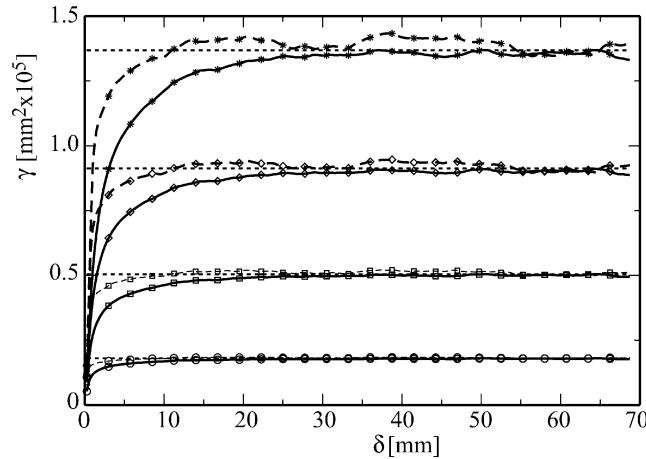
Fig. 4. Semivariograms of aperture fields corresponding to shift amplitudes u equal to: (0.25 mm, circles), (0.5 mm, squares), (0.75 mm, diamonds) and (1 mm, asterisks). "δ" corresponds to the "lag". Dashed lines: $\gamma_{//}$ (correlation along the direction of $\vec{u}$). Solid lines: $\gamma_\perp$ (correlations in the direction perpendicular to $\vec{u}$). Horizontal dotted lines correspond to twice the aperture variance for the same u values.

Fig. 4 displays the semivariances $\gamma_\perp$ and $\gamma_{//}$ for aperture fields computed from the same experimental surface profile map $h(\vec{r})$, but for different magnitudes of the shear displacements $\vec{u}$. For small magnitudes of $\vec{\delta}$, the apertures at $\vec{r}$ and $\vec{r} + \vec{\delta}$ are very similar (high spatial correlation at short distances) and γ is small. As $|\vec{\delta}|$ increases, so does γ, because the spatial correlation in aperture decreases. As $|\vec{\delta}|$ increases further, to a value higher than the correlation length of the aperture field, the apertures at $\vec{r}$ and $\vec{r} + \vec{\delta}$ become uncorrelated. Then, based on Eq. (4), $\gamma_\perp$ and $\gamma_{//}$ should reach the same saturation value, equal to twice the aperture variance (σ_a):

$$\sigma_a = \langle [a(x, y) - a_0]^2 \rangle \tag{5}$$

The values of σ_a, corresponding to the different shear amplitudes $|\vec{u}|$, are plotted as horizontal dashed lines in Fig. 4 and agree with the asymptotic values of both $\gamma_\perp$ and $\gamma_{//}$ at high $|\vec{\delta}|$ values. Also, as previously shown by Auradou et al. (2005), σ_a increases with the magnitude of the shear displacement $|\vec{u}|$. In the range of $|\vec{u}|$ values shown in Fig. 4, we can verify experimentally that $\sigma_a = Au^{2\zeta}$ with a best fit corresponding to $\zeta = 0.75$ and $A = (137{,}000)^{2(1-\zeta)}$.

Even though the asymptotic values of $\gamma_\perp$ and $\gamma_{//}$ are the same at large $|\vec{\delta}|$ values for a given shear displacement $|\vec{u}|$, the way in which they reach this saturation value differs greatly for the two semivariances, due to the anisotropy of the fracture aperture field. The semivariance $\gamma_\perp$, corresponding to $\vec{\delta}$ perpendicular to $\vec{u}$, never exceeds its saturation value and reaches it in an overdamped way. On the other hand, $\gamma_{//}$ ($\vec{\delta}$ parallel to $\vec{u}$) displays a small overshoot, reflecting a local anticorrelation. These different behaviors result directly from the large-scale anisotropic structures observed in Fig. 3. Let us consider the aperture at two points separated by a small distance $\vec{\delta}$ perpendicular to the shear displacement (and therefore parallel to the channel structures); both will most likely be either above or below the average aperture; for instance, if they are inside the same large-scale high or low velocity channel. The corresponding value of aperture semivariance will then be less than σ_a. On the other hand, two points with a separation $\vec{\delta}$ parallel to $\vec{u}$ have a higher probability of corresponding to different structures of the binary images; some degree of anticorrelation can therefore be expected.

Let us now investigate the parameters determining the behavior of γ with δ for different values of the ratio δ/u. To achieve this, we tried to collapse the different curves of Fig. 4 onto master curves. In Fig. 5, $\gamma_\perp$ and $\gamma_{//}$ are normalized by $Au^{2\zeta}$, which represents their asymptotic value for
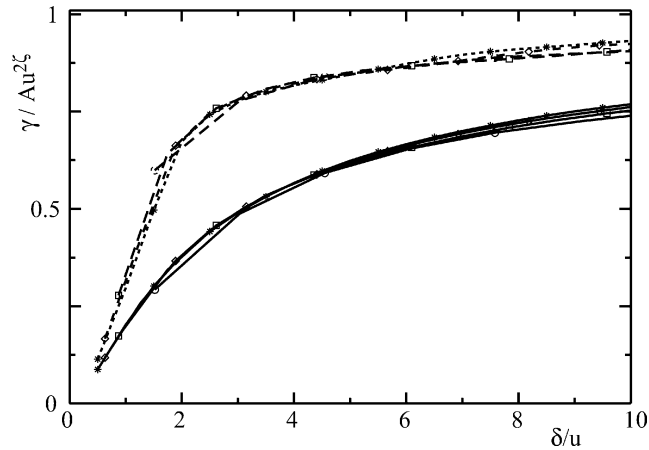
Fig. 5. Semivariograms of aperture fields normalized by $Au^{2\zeta}$ ($\zeta = 0.75$ and $A = (137,000)^{2(1-\zeta)}$) as a function of the normalized lag δ/u. Shear amplitude u values: (0.25 mm, circles), (0.5 mm, squares), (0.75 mm, diamonds) and (1 mm, asterisks). Dotted and dashed lines: $\gamma_{//}$ (correlation along the direction of $\vec{u}$). Solid lines: $\gamma_{\perp}$ (correlation in the direction perpendicular to $\vec{u}$). Note that the range of values on the horizontal axis is narrower than in Fig. 4 so that the overshoot effect is not visible.

large displacements. The horizontal scale, δ/u, is a natural reduced coordinate (see Plouraboué et al., 1995). These two normalizations allow us to collapse the different results into two independent master curves, corresponding to the two orientations of $\vec{\delta}$ with respect to $\vec{u}$. This demonstrates that, in all cases, the characteristic distance over which the aperture field becomes uncorrelated is proportional to the magnitude of the shift u. In addition, the ratio between this distance and u is significantly larger for $\vec{\delta}$ oriented perpendicular to the direction of shear. This fact remains valid even when the actual values of both correlation distances may vary significantly from one sample to another. Fig. 5 also shows that, for small lag values ($\delta/u \ll 1$), the semivariograms increase linearly with δ/u ($\gamma/u^{\zeta} \propto \delta/u$), which indicates that the random field is not as smooth as in a Gaussian covariance function for which $\gamma \propto \delta^2$.

At large distances ($\delta \gg u$), the semivariance γ still displays large fluctuations, with excursions above and below the asymptotic value σ_a. These can been seen in Fig. 6, which shows the normalized deviations $(\gamma - \bar{\gamma})/\bar{\gamma}$ of γ from its average value $\bar{\gamma}$ over all distances $\delta > 15$ mm. It
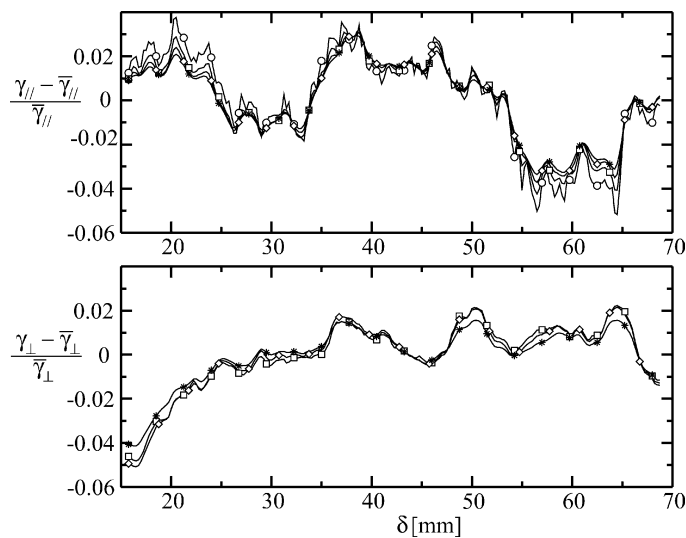

Fig. 6. Variations of $(\gamma_{//}/\bar{\gamma}_{//} - 1)$ (top) and $(\gamma_{\perp}/\bar{\gamma}_{\perp} - 1)$ (bottom) normalized by u^{ζ} ($\zeta = 0.75$) as a function of lag δ. Shear amplitudes u: (0.25 mm, circles), (0.5 mm, squares), (0.75 mm, diamonds) and (1 mm, asterisks).

is evident that the fluctuations coincide provided that δ is used as the horizontal scale (and not the normalized lag δ/u as in Fig. 5), which suggests that these variations reflect the large-scale, underlying structures displayed in Fig. 3, and that their location is independent of the magnitude of the shear displacement. The fluctuations will, however, vary greatly from one sample to another. The variation of the amplitude of the fluctuations with u is not trivial: the normalized deviations $(\gamma - \bar{\gamma})/\bar{\gamma}$ had to be divided by u^ζ to obtain the collapse shown in Fig. 6, which suggests that there is some influence of the local self-affine structure on these fluctuations. If they were only due to the large-scale channels, then the normalized deviations would be proportional to u.

4. Correlation between aperture field and displacement fronts

This section is devoted to the geometry of the front between two miscible fluids (or equivalently to the dispersion of a tracer) within a single fracture. Several mechanisms contribute to the spreading of the front (or the tracer). These include molecular diffusion, Taylor dispersion as a result of the velocity profile in the fracture gap, and geometrical dispersion caused by the velocity variations between different flow lines in the mean fracture plane; see Drazer and Koplik (2002) and Drazer et al. (2004) for a discussion of the contribution of the above-mentioned mechanisms to tracer dispersion.

We will consider only the last mechanism, allowing us to simplify the problem to a two-dimensional flow field $v(x, y)$ obtained by averaging the three-dimensional velocities over the gap of the fracture, $v(x, y) = \langle v(x, y, z) \rangle_z$. The pressure gradient inducing the flow and the resulting mean velocity are parallel to the x-axis, and the front (or the tracer) is initially located at the inlet of the fracture on a line parallel to the y-axis. Below, we analyze the development of the front (or the tracer flow lines) with time, assuming that it moves at the local flow velocity, and present a simple analytical model accounting for the geometry of the front.

The following model is based on the results discussed above, namely that the aperture field in the fracture is structured into channels perpendicular to the shear displacement $\vec{u}$. For a mean flow parallel to these channels, the tracer particles follow paths that are only weakly tortuous; furthermore, the variations in their velocity along these flow paths are small compared to the velocity contrasts between the different channels. Under these assumptions, the velocity of a particle located at a distance y satisfies: $\vec{v}(x, y) \approx v(y)\vec{n}_x$, where $\vec{n}_x$ is a unit vector parallel to the mean flow. Note also that there are no contact points between the walls of the fractures we have used, which allows us to avoid considering highly tortuous flow lines in the vicinity of these points. For each channel the velocity $\vec{v}(y)$ is related to the pressure gradient dP/dx by Darcy's equation:

$$\vec{v}(y) = -\frac{a^2(y)}{12\mu}\frac{dP}{dx}\vec{n}_x \tag{6}$$

in which $a(y)$ is the equivalent (or hydraulic) aperture of the channel. Then, particles starting at different positions y at the inlet move at different velocities, $v(y)$, and their distance x from the inlet at time t after the start of injection satisfies $x(t) = v(y)t$; the mean front position then moves at the average flow velocity with $\bar{x}(t) = \langle v(y) \rangle_y t$; combining these two latter relations with Eq. (6) we obtain:

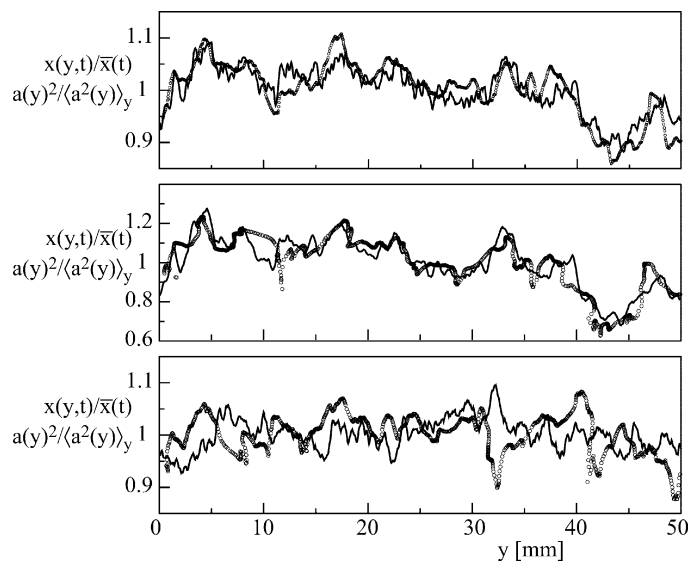$$\frac{x(y, t)}{\bar{x}(t)} = \frac{a^2(y)}{\langle a^2(y) \rangle_y} \tag{7}$$

Fig. 7. Comparison of normalized front profiles $x(y, t)/\bar{x}(t)$ (circles) and normalized apertures $a(y)^2/\langle a^2(y)\rangle_y$ (solid lines) as a function of the distance y across the flow. Top graph: flow normal to shear displacement $\vec{u}$ with $u = 0.2$ mm. Middle graph: flow normal to shear displacement $\vec{u}$ with $u = 0.6$ mm. Bottom graph: flow parallel to $\vec{u}$ for $u = 0.6$ mm (the vertical scale of the solid line has been amplified by a factor of 10). For all graphs, the mean fracture aperture is 1 mm and the horizontal dimensions of the fracture are 51.2 mm × 51.2 mm.

Finally, previous studies have shown that, for relatively small aperture fluctuations, the hydraulic aperture is about equal to the geometrical mean of the apertures (Brown, 1987; Zimmerman et al., 1991). This suggests that $a(y)$ can be approximated by the average of the local apertures along the x direction, with $a(y) = \langle a(x, y)\rangle_x$. The validity of this assumption has been tested by comparing the shape of the front $x(y, t)$ given by the numerical simulations using the lattice Boltzmann method against the variations of the effective aperture squared, $a^2(y)$. The comparison is shown in Fig. 7 where the normalized displacements, $x(y, t)/\bar{x}(t)$, of particles released at $x = 0$ are plotted as a function of the position y, together with the normalized square of the aperture averaged in the direction parallel to the flow: $a^2(y) = \langle a^2(y)\rangle_y$. When the mean flow is perpendicular to the shear displacement, the variations with y of the normalized position of the particles and that of the normalized square aperture are very similar, both for $u = 0.2$ mm and $u = 0.6$ mm (Fig. 7, top and middle graphs). The small differences may be due, in part, to the effect of viscous entrainment between adjacent flow channels caused by viscous diffusion. On the other hand, when the mean flow is parallel to $\vec{u}$ (bottom graph), there is very little correlation between the two curves and the amplitudes of the variations are very different (note that the curve corresponding to $a^2(y)/\langle a^2(y)\rangle_y$ has been magnified by a factor of 10). These differences reflect, and confirm, the anisotropy of the aperture field induced by the shear displacement $\vec{u}$.

The assumptions underlying the above model and, in particular, Eq. (7) are indeed only valid if the flow field can be described as parallel channels with a length of the order of that of the fracture. For a mean flow perpendicular to $\vec{u}$, the model represents a valid approximation; the aperture of the flow channels displays long-range correlations and particles are convected along each channel with a slightly fluctuating velocity. Note that, in this case, the global width of the front in the x-axis increases linearly with time, while for dispersive processes it increases with the square root of time. This difference results from the fact that the correlation length of the velocity of fluid particles is of the same order as the total path length along the fracture; a dispersive regime can only be reached if the correlation length is much smaller than the fracture size. For flow parallel to
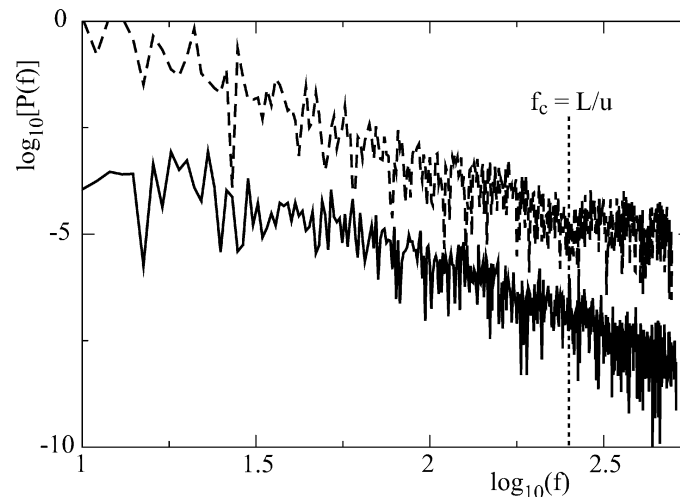
Fig. 8. Plot of the logarithm of the power spectrum $P(f)$ of the deviations of the front displacement $x(y, t)$ (dashed line at the top) and of the squared effective aperture $a^2(y)$ (solid line at the bottom) as a function of the logarithm of the dimensionless spatial frequency $f = L/x$ (shear displacement $u = 0.2$ mm, mean aperture $a_0 = 1$ mm, fracture size $L = 51.2$ mm). The curves are shifted vertically relative to each other for clarity. The vertical dotted line indicates the cutoff frequency $f_c = L/u$ of the self-affine domain for the upper curve.

$\vec{u}$, the flow lines are more tortuous and velocity fluctuations are enhanced. In this case, the model no longer describes the geometry of the front and its width parallel to the mean flow is reduced.

Further information is obtained by performing Fourier transforms of the deviations of the local displacement of the front, $x(y, t)$, and of the square of the estimated effective aperture, $a^2(y)$, from their mean values (the mean flow is perpendicular to the shear displacement $\vec{u}$). The resulting power spectra are shown in Fig. 8; as could be expected from the qualitative analysis of the curves of Fig. 7, both spectra are similar up to dimensionless frequencies f of the order of $f_c = L/u$ (where L is the fracture length). In fact, for wavelengths smaller than the shear displacement u, only $a^2(y)$ displays self-affine properties while the small-scale details of the flow field are determined by other factors such as viscous stresses.

5. Discussion and conclusions

The experiments and numerical simulations performed as part of this study revealed new features of flow and transport in rough fractures. We have specifically studied the influence of a relative shear displacement of complementary wall surfaces on the fracture aperture field, as well as on the transport properties of the fracture. This has particular relevance to geothermal reservoirs, where high-pressure fluid injection frequently induces relative displacements of the fracture walls. Following previous experimental results, the rough fracture walls have been assumed to display a self-affine geometry.

First, we have shown that the relative shear displacements $\vec{u}$ induce an anisotropy of the fluid flow field that reduces the permeability for flow parallel to $\vec{u}$ and enhances it in the perpendicular direction. This may account, in part, for the permeability enhancement in some sheared zones of the reservoir. These changes are well predicted by assuming the development, in the aperture field, of large ridges perpendicular to the shear direction and extending over the full length of the fracture; these ridges act as parallel channels enhancing flow parallel to them and reducing transverse velocity fluctuations. The resulting anisotropy has been confirmed quantitatively by computing semivariograms of the aperture fields, which display a correlation length proportional

to the magnitude of the shear displacement for a given orientation and significantly larger in the direction perpendicular to the shear.

A second important result is the strong correlation between the roughness of the fracture walls and the geometry of the displacement fronts, particularly for flow perpendicular to $\vec{u}$; these fronts have a self-affine geometry characterized by the same exponent as that characterizing the fracture walls. Also, for a mean flow perpendicular to $\vec{u}$, the front width is found to increase linearly with distance. This reflects a channeling parallel to the mean flow, resulting in weak velocity fluctuations along the paths of the fluid particles. One further important consequence is that, in this case, the front geometry can be estimated accurately from the variations of the square of the aperture averaged in the direction parallel to the mean flow.

These results raise a number of fundamental points that will be considered in future studies. First, we might expect the spatial correlations of the velocity field to decay eventually, leading to a normal Gaussian dispersion process at long distances. This has not been observed in our laboratory or numerical studies, and we have currently no estimate of the corresponding correlation length. The channeling effect might also result in the movement of some fluid packets at a velocity substantially faster than the average flow velocity, at least in transient regimes of duration shorter than the time necessary to sample the flow variations inside the fracture. The channeling effect may therefore strongly affect heat exchange between the rock and the flowing fluid, as well as the transport of chemical species involved in the mineral dissolution–deposition processes that frequently occur in fractured geothermal systems such as that at Soultz. In the case of a channelized flow, for instance, the variability of the residence times in the various flow channels may result in lower fluid production temperatures than if no channelization was present.

The results of studies on flow and solute dispersion in rough fractures, such as we have just presented, represent the first step towards the modeling of other transport properties such as heat transfer or dissolution–precipitation of minerals in HDR and other fractured geothermal reservoirs.

Acknowledgments

References

Auradou, H., Hulin, J.P., Roux, S., 2001. Experimental study of miscible displacement fronts in rough self-affine fractures. Phys. Rev. E 63, 066306.

Auradou, H., Drazer, G., Hulin, J.P., Koplik, J., 2005. Permeability anisotropy induced by the shear displacement of rough fracture walls. Water Resour. Res. 41, W09423, doi:10.1029/2005WR003938.

Bouchaud, E., 2003. The morphology of fracture surfaces: a tool for understanding crack propagation in complex materials. Surf. Rev. Lett. 10, 797–814.

Brown, S.R., 1987. Fluid through rock joints: the effect of surface roughness. J. Geophys. Res. 92 (82), 1337–1347.

Dezayes, Ch., Genter, A., Gentier, S., 2004. Fracture network of the EGS geothermal reservoir at Soultz-sous-Forêts (Rhine Graben, France). Geotherm. Resour. Council Trans. 28, 213–218.

Drazer, G., Koplik, J., 2000. Permeability of self-affine rough fractures. Phys. Rev. E 62, 8076–8085.

Drazer, G., Koplik, J., 2002. Transport in rough self-affine fractures. Phys. Rev. E 66, 026303.

Drazer, G., Auradou, H., Koplik, J., Hulin, J.P., 2004. Self-affine fronts in self-affine fractures: large and small-scale structure. Phys. Rev. Lett. 92, 014501.

Evans, K., Moriya, H., Niitsuma, H., Jones, R.H., Phillips, W.S., Genter, A., Sausse, J., Jung, R., Baria, R., 2005. Microseismicity and permeability enhancement of hydrogeologic structures during massive fluid injections into granite at 3 km depth at Soultz H.D.R. site. Geophys. J. Int. 160, 388–412.

Feder, J., 1988. Fractals. Physics of Solids and Liquids. Plenum Press, New York, NY, USA, p. 283.

Genter, A., Castaing, C., Dezayes, Ch., Tenzer, H., Traineau, H., Villemin, T., 1997. Comparative analysis of direct (core) and indirect (borehole imaging tools) collection of fracture data in the Hot Dry Rock Soultz reservoir (France). J. Geophys. Res. 102 (B7), 15419–15431.

Gentier, S., Lamontagne, E., Archambault, G., Riss, J., 1997. Anisotropy of flow in a fracture undergoing shear and its relationship to the direction of shearing and injection pressure. Int. J. Rock Mech. Min. Sci. 34 (3–4), 412.

Kitanidis, P.K., 1997. Introduction to Geostatistics: Applications in Hydrogeology. Cambridge University Press, Cambridge, MA, USA, p. 249.

Plouraboué, F., Kurowski, P., Hulin, J.P., Roux, S., Schmittbuhl, J., 1995. Aperture of rough cracks. Phys. Rev. E 51 (3), 1675–1685.

Sausse, J., 2002. Hydromechanical properties and alteration of natural fracture surfaces in the Soultz granite (Bas-Rhin, France). Tectonophysics 348 (169), 185.

Yeo, I.W., De Freitas, M.H., Zimmerman, R.W., 1998. Effect of shear displacement on the aperture and permeability of a rock fracture. Int. J. Rock Mech. Min. Sci. 35 (8), 1051–1070.

Zimmerman, R.W., Bodvarsson, G.S., 1996. Hydraulic conductivity of rock fractures. Transp. Porous Media 23, 1–30.

Zimmerman, R.W., Kumar, S., Bodvarsson, G.S., 1991. Lubrication theory analysis of the permeability of rough-walled fractures. Int. J. Rock Mech. Min. Sci. Geomech. Abstr. 28 (4), 325–331.